Journal of Manufacturing Processes 124 (2024) 1471–1484

Contents lists available at ScienceDirect

Journal of Manufacturing Processes

journal homepage: www.elsevier.com/locate/manpro

On the modelling and experimental study of CO_2 laser ablation on resin-bond diamond grinding wheels: Understanding the effect of processing parameters on the time-dependent temperature field

Ke Ge Xie [a,b,1], Adam George Antrum Rushworth [b,c,*,1], Hao Chen [b,*], Jinyi Li [d]

[a] Department of Mechanical and Energy Engineering, Southern University of Science and Technology, Shenzhen 518055, China
[b] Department of Mechanical, Materials & Manufacturing Engineering, University of Nottingham Ningbo China, Ningbo 315100, China
[c] Control Systems Lab, University of Nottingham Ningbo China, Ningbo 315100, China
[d] School of Aerospace, University of Nottingham Ningbo China, Ningbo 315100, China

ARTICLE INFO

Keywords:
Modelling
CO_2 Laser
Diamond grinding wheels
Temperature field distribution

ABSTRACT

The need for the precise dressing of diamond abrasive tools by laser has been highly emphasised but determining controllable material removal strategies for precise laser processing remains challenging due to the complex interaction between the composite abrasive materials and the laser beam. To fill this gap, an innovative simulation model pertaining to the laser ablation process has been devised to study the temporal evolution of the temperature field distribution within the ablation zone during processing, alongside monitoring the alterations in ablation depth along the feed direction. The laser spot focus size and the cross-section laser energy intensity distribution along the beam propagation direction, as well as the dynamic, unsteady-state heat conduction and convection, are considered in this model. Based on the simulation results, the ablation law regarding temperature field distribution and ablation depth variation with laser power and feed rate is revealed. It is shown that the laser power has a limited impact on the shape of temperature field distribution, but the core temperature of the heat-affected zone increases with laser power. The feed rate affects mainly the distribution range of the heat-affected zone and the range shrinks with the feed rate. It is revealed that a higher laser power with a matched higher feed rate is highly expected to optimise the ablation. Finally, the simulation results are experimentally validated and reasonable agreements are obtained. The work provides numerical and experimental evidence to evaluate the time-dependent temperature distribution during the laser ablation process.

1. Introduction

Diamond abrasive tools with resin bond agency have been widely used in industrial applications because of their superior performance in wear-resistance [1], elasticity [2], and thermal conductivity [3], especially in developed countries. However, the dressing strategies for diamond abrasive tools are still lacking as the super-hard abrasives and the fragile impact resistance make it hard to dress them in an efficient and low-cost way [4]. Laser processing is a promising technology, but it remains challenging to remove the target materials in a controllable way for the wide range of failure temperatures of the tools' ingredients [5]. Previously, various work has been done using laser processing technology and significant progress has been made, including experimental [6] and simulation [7] work.

Among the experimental research, Walter et al. [8] emphasised the unique advantages of thermal methods, including the high possibility of fabricating macro, *meso*, and micro simple/complex structures. Rabiey [9] made blind holes on a CBN grinding wheel surface using an Nd: YAG laser to reduce the contact area between the grinding wheel and the workpiece: roughly 5 mm ablation depth and a 500 μm spot diameter were obtained. Zhang et al. [10] studied the evolution of micro/nano-structural arrays on crystalline silicon carbide, finding the irradiated surface evolves from a near-damage-free zone to one with a recast layer and thermal-induced micro-cracks. Cai et al. [11] carried out experiments with a femtosecond laser (where the power employed is at a hundred mW level) and demonstrated that the diamond ablation depth changes law with laser power and processing time. Li et al. [12] investigated the ablation law of a continuous CO_2 laser and based on their

* Corresponding authors.
E-mail addresses: Adam.Rushworth@nottingham.edu.cn (A.G.A. Rushworth), Hao.Chen@nottingham.edu.cn (H. Chen).
[1] These authors contributed equally to this work.

https://doi.org/10.1016/j.jmapro.2024.07.007
Received 28 January 2024; Received in revised form 17 June 2024; Accepted 2 July 2024
Available online 13 July 2024

derived law, generated complex textures on diamond resin bond grinding wheels, with a minimum of about 800 μm width and 250 μm depth slots. Similarly, Xie et al. [13] studied the effect of the line overlap rate of a CO_2 laser beam on the ablated bottom shape, producing non-flat surfaces on the grinding wheels. Rushworth et al. [14] explored the ablation law of a 2000 W fibre laser and established a predictive model for generating the precise profiled grinding wheel. Another avenue for thermal texturing of abrasive tools can be a series of studies performed by Butler-Smith et al. [15] where the pulse laser was used to ablate thick-film CVD diamond so that preferential micro-grinding arrays in rectangular, triangular, and hexagonal shapes could be generated.

In terms of the simulation works, Parthiban et al. [16] used the response surface method to model the CO_2 laser-cutting process. They showed that the finished product quality mainly depends on the input parameters such as laser beam power, cutting speed and assist gas pressure. Thanks to the least complex of these empirical models, a convenient prediction result can be easily achieved with the proper design of the experiment. Therefore, many essential works have been done based on this model to study the key machining factors affecting the experimental results despite the imperfect empirical model. Despite the usefulness of the model, it lacks an understanding of the machining process from the scientific level. Therefore, few works regarding the laser ablation process have been published based on the empirical model.

However, the most popular research works were conducted using numerical methods, including titanium-matrix composites [17] and Vivo bio-tissues [18]. Orimi et al. [19] used the COMSOL software to build a model considering laser parameters like laser power, sampling rate, and optomechanical parameters to predict the machined path's roughness, depth, and thickness. The simulation results are in good agreement with experimental outcomes, which can be used to estimate the effect of the process parameters before the machining. *Ma* et al. [20] proposed a Finite Element Analysis (FEA) simulation model for the Pulsed Laser Ablation (PLA) in mechanical processing. This model accurately described the energy distribution on component surfaces, which was crucial for further study of the ablation topography. By considering the energy distribution of the laser beam model and element birth and death technique, Moradi et al. [21] developed a numerical simulation of the CO_2 laser cutting process of polycarbonate sheets by a finite element method. The results show the effectiveness of the model when the death of the element was used. Otto and Schmidt [22] presented a new but still quite universal numerical simulation model for laser material processing. Simulation results on several processes like laser beam deep penetration welding, drilling or cutting were presented. Finally, an outlook on planned further developments was given, and possible model applications were discussed. Notably, the numerical model was the most used in the study, and significant progress has been made thanks to the many reliable commercial application software that have been developed to make it friendly to use. With the application of the model, the micro-behaviours within the laser-material interaction area can be observed and studied. Nevertheless, it required a lot of processing power, and the accuracy and floatability were relatively large based on the conditions such as the modelling level of the researcher and the treatment of the boundary conditions and load cases.

There was also research that explored the analytical methods for laser ablation modelling. An analytical model was built with a number of simplifications and assumptions. It was a function based on the theoretical relationship calculated by analysing the physical mechanism and establishing the appropriate physical model of the object. Criales et al. [23] investigated the effects of varying process parameters on the ablated topographies and the resultant microchannel dimensional quality in the polymethyl methacrylate by analytical modelling and experiment. Cha and Axinte [7] developed a transient thermal model of nanosecond pulsed laser ablation to study the effect of heat accumulation during the processing of semi-transparent ceramics. Two most relevant research works regarding non-metallic inhomogeneous materials analytical modelling have also been found. Peligrad et al. [24] built an analytical model for the CO_2 laser glazing of inhomogeneous workpieces (clay tiles) based on parabolic melt pool geometry. The theoretical results showed a close correlation with the experimental when the parameter $P_L/\sqrt{dv}$ was less than 15 W/mm/s. Salim et al. [25] further developed the analytical model by combining the empirical element with the model and carried out experiments on concrete surface ablation with a continuous CO_2 laser. As a result, the new model showed a high agreement (96 %) with the experiments. Although the results of the improved model were pleasing for non-metallic inhomogeneous materials, they were validated under limited conditions that included a maximum laser power of 65 W and an ablation depth of 1.6 mm. Meanwhile, due to the idealised assumptions of the model, it could not be generally applied.

Based on the understanding of the previous research, they showed great work had been done by experiments to explore the dressing technologies for various grinding wheels and significant progress had been made. However, these experimental works usually determined the proper processing parameters using trial and error, which was inefficient and costly. Meanwhile, it was hard to understand the real-time laser ablation process and to make the ablation results predictable. Notably, these defects could be well solved by the simulation method. Nevertheless, although much simulation work regarding laser ablation processes had been done, from empirical models, via numerical models, to analytical models, no simulation models studied the time-dependent temperature field distribution in the ablation zone, especially no research studied the laser processing on resin-bond diamond grinding wheel featuring ingredients with multiple and varied failure temperatures.

To address this gap, a model was developed firstly to account for the energy distribution of the beam spot along the laser beam propagation direction as well as the laser energy transferred to the ambient atmosphere in different scenarios. Secondly, the time-dependent temperature field distribution in the ablation zone was analysed and the changes in the ablation depth with processing parameters were investigated. Finally, experimental and simulated results were compared, and optimal processing strategies were recommended. These findings make a valuable contribution to the existing body of research in this field.

2. Modelling process

2.1. Model description

In the ablation process, a laser beam with intensive energy radiated on a grinding wheel's surface and moved along with the wheel rotation (see Fig. 1a). The target materials absorbed the energy, deteriorated, and formed a slot. As a result, the following factors should be included in the modelling:

The laser intensity accorded with an axisymmetric super-Gaussian model [26]. Therefore, the laser beam energy distribution exerted a significant influence on the calculation, which finally affected the prediction of the temperature field (here especially represents the area suffered from temperature rising caused by laser irradiation) distribution. In line with the facilities employed in this study, the laser beam intensity followed the axisymmetric super-Gaussian distribution model with flat-top function located in the beam waist (as shown in Fig. 1b & c A-A) and evolved into a standard Gaussian function along with the beam propagation (as shown in Fig. 1b & c B-B and C-C). Besides, after the laser beam penetrated the workpiece surface, the intensity attenuated due to the materials absorbing energy and reflecting some of the energy to the surroundings.

The relationship between the laser processing parameters and the output temperature field should be considered because a control strategy of selecting the processing parameters was feasible to control the heat-affected zone online for industrial applications. Among these

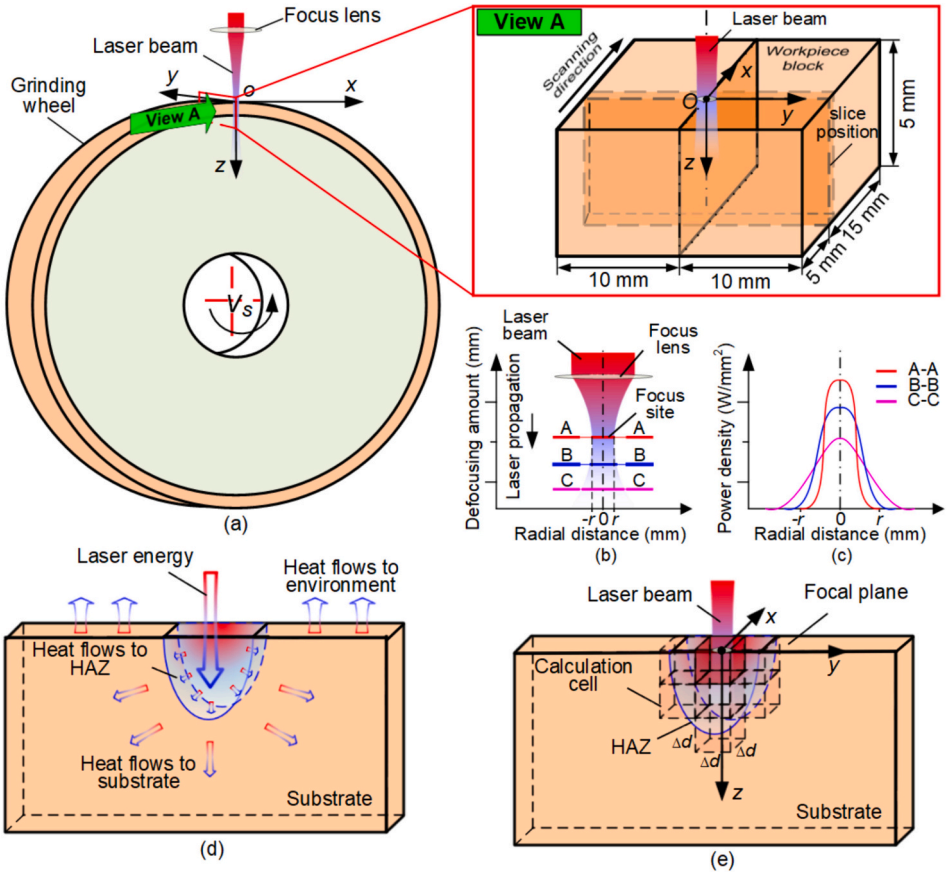

Fig. 1. Ablation process description. (a) Left view and (b) front view of the grinding wheel; (c) top view of the sample; (d) lateral section and (e) cross-section of the slot on the sample.

processing parameters, feed rate and laser power were the two most important and convenient factors to be controlled online by an electromechanical system.

This model was generally based on discretising the entire domain into cubic unit cells. The calculation domain (see Fig. 1a View A) contains the initial relative position information of the laser beam and the workpiece block with dimensions. For each slice (see Fig. 1d), the laser beam radiates through the target materials and brings heat to the heat-affected zone. At the surface of the substrate, the heat was conducted to the ambient atmosphere through heat convection and radiation. Moreover, at the inner of the substrate, the energy was conducted to the around substrate by conduction and finally to the surrounding ambience.

With the principle above, (i) the isotherm for the temperature field distribution dominated by laser energy was calculated first to reveal the approximate region of the heating zone, and (ii) the ablation depth (the position of the lowest temperature point which could cause the failure of the materials for each time step) is calculated.

2.1.1. *Isotherm for temperature field distribution calculation*

The temperature field was solved to predict the shape of the ablated area. To calculate the entire temperature field in the workpiece block, the computing domain was separated into finite small cubic cells with an edge length of Δd. Each position of the cell was defined as (x, y, z) in the global coordinate system (see Fig. 1e) and had a changing temperature as it absorbed the laser energy and transferred the energy to adjacent cells or the atmosphere.

The cell temperature can be expressed as Eq. (1) when being irradiated by a laser beam.

$$T_{x,y,z,t+\Delta t} = T_{x,y,z,t} + \frac{Q_l}{\rho(\Delta d)^3 C_\rho^*} \tag{1}$$

where $T_{x,y,z,t}$ is the spatial transient temperature, ρ is the material density, C_ρ^* is the modified specific heat capacity of the composite, and Q_l is the laser energy input. All properties of the composite are hypothesised constant.

The temperature computed through Eq. (1) can be refined by including heat conduction behaviours, containing (i) heat conduction through higher temperature to low per unit time Δt as described in Eq. (2) [27]

$$C_p \frac{\partial T^{in}_{x,y,z,t+\Delta t}}{\partial t} = k\left(\frac{\partial^2 T_{x,y,z,t}}{\partial^2 x} + \frac{\partial^2 T_{x,y,z,t}}{\partial^2 y} + \frac{\partial^2 T_{x,y,z,t}}{\partial^2 z}\right) \tag{2}$$

where k is the conductivity, and $T^{in}_{x,y,z,t+\Delta t}$ is the temperatures of the interior cubic cells, and (ii) the convection and radiation transfer from the workpiece surface to the environment can be expressed as Eq. (3) [28]

$$h_n\left(T^w_{x,y,z,t+\Delta t} - T_\infty\right) = -k\left(\nabla T_{x,y,z,t} \cdot \vec{n}\right) \tag{3}$$

where $\nabla T_{x,y,z,t}$ is the temperature gradient of the boundary cell and interior cell, $\vec{n}$ is the normal vector of the surface, h_n is the combined convection and radiation coefficient, $T^w_{x,y,z,t+\Delta t}$ is the boundary temperature of the cell, and T_∞ is the environmental temperature.

It is worth mentioning that the solutions of heat transfer in Eqs. (2)–(3) involve a numerical finite difference method is proposed by Holman.

Eq. (2) depicts conduction inside the material (see red cells in Fig. 2)

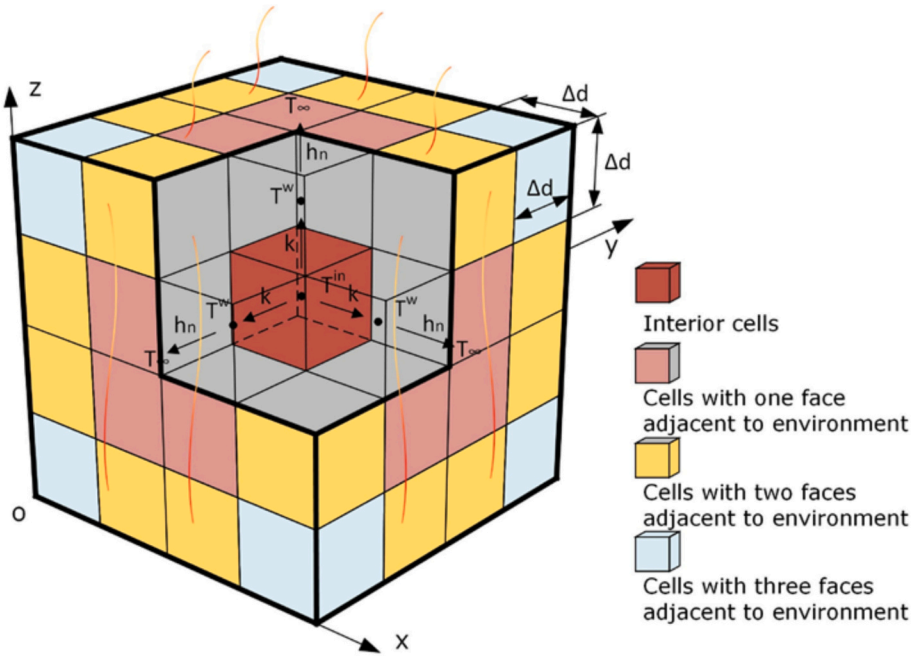

Fig. 2. Diagram of the different cases in the heat transfer solution [31].

and can be numerically solved by Eq. (4) [27]

$$T^{in}_{x,y,z,t+\Delta t} = \frac{k\Delta t}{\rho C_\rho (\Delta d)^2}\left(T_{x-\Delta d,y,z,t} + T_{x+\Delta d,y,z,t} + T_{x,y-\Delta d,z,t} + T_{x,y+\Delta d,z,t} + T_{x,y,z-\Delta d,t} + T_{x,y,z+\Delta d,t} - 6T_{x,y,z,t}\right) + T_{x,y,z,t} \tag{4}$$

Eq. (3) describes convection and radiation between boundary cells and the environment, which can be solved based on the three different cases related to the number of faces exposed to the external environment:

In Case (i), where exactly one cell face is adjacent to the environment in either x, y, or z direction (see the light red cells in Fig. 2), Eq. (3) can be numerically solved by Eq. (5) [27]

$$T^{w}_{x,y,z,t+\Delta t} = \frac{k\Delta t}{\rho C_\rho (\Delta d)^2}\left(\frac{2h_n\Delta d}{k}\left(T_\infty - T_{x,y,z,t}\right) + 2T_{x-\Delta d,y,z,t} + T_{x,y-\Delta d,z,t} + T_{x,y+\Delta d,z,t} + T_{x,y,z-\Delta d,t} + T_{x,y,z+\Delta d,t} - 6T_{x,y,z,t}\right) + T_{x,y,z,t} \tag{5}$$

In Case (ii), where exactly two cell faces are adjacent to the environment in either combination of the direction (see the yellow cells in Fig. 2), Eq. (3) can be numerically solved by Eq. (6) [27]

$$T^{w}_{x,y,z,t+\Delta t} = \frac{2k\Delta t}{\rho C_\rho (\Delta d)^2}\left(\frac{2h_n\Delta d}{k}\left(T_\infty - T_{x,y,z,t}\right) + T_{x-\Delta d,y,z,t} + T_{x,y-\Delta d,z,t} + T_{x,y,z-\Delta d,t} + T_{x,y,z+\Delta d,t} - 4T_{x,y,z,t}\right) + T_{x,y,z,t} \tag{6}$$

In Case (iii), where three faces are adjacent to the environment (see the light blue cells in Fig. 2, Eq. (3) can be numerically solved by Eq. (7) [27]

$$T^{w}_{x,y,z,t+\Delta t} = \frac{2k\Delta t}{\rho C_\rho (\Delta d)^2}\left(\frac{2h_n\Delta d}{k}\left(T_\infty - T_{x,y,z,t}\right) + T_{x-\Delta d,y,z,t} + T_{x,y-\Delta d,z,t} + T_{x,y,z-\Delta d,t} - 3T_{x,y,z,t}\right) + T_{x,y,z,t} \tag{7}$$

The laser energy Q_l in Eq. (1) is computed by the definition of laser energy absorbed by the workpiece in a specific area and time as expressed in Eq. (8) [29]

$$Q_l = \beta(\Delta d)^2 \Delta t \eta I \tag{8}$$

where β is the absorptivity of material, Δt is the time step for computing, η is the attenuation function, and I is the laser intensity. The processing parameters affects the energy absorption by the way (i) the feed rate determined the dwell time causing heat accumulated and (ii) the laser power determined the laser intensity varying the energy in unit area and time.

The attenuation function η depict the remaining laser intensity I after being absorbed by the workpiece along the penetrating direction and can be expressed as Eq. (9) [30]

$$\eta = exp[-C_{ab}(h-z)] \tag{9}$$

where h is the height of the substrate, C_{ab} is the absorption coefficient.

The laser intensity I in Eq. (8) obeyed the super-Gaussian distribution that can be expressed by Eq. (10) [26]

$$I = \frac{2^{1/n} nP}{\pi r^2 \Gamma\left(\frac{1}{n}\right)} exp\left[-2\left(\frac{(x-x_l)^2 + (x-x_l)^2}{r^2}\right)^n\right] \tag{10}$$

where P is the laser power, r is the radius of the laser beam, n is the super-Gaussian order, and Γ is the Gamma function. Based on the above, the temperature in each cell can be solved by the heating effect of Eq. (1) and heat transfer of Eqs. (2) and (3).

2.1.2. Ablation depth calculation

As most of the previous studies have investigated the ablation depth by the empirical model, in this study, the ablation depth is calculated from the analytical solution, which can be written as Eqs. (11)–(13).

$$T_{y,z,t+\Delta t} = T_{x,y,z,t+\Delta t}(x = x_0 + xt) \tag{11}$$

$$T_{z,t+\Delta t} = T_{y,z,t+\Delta t}(y = 0) \tag{12}$$

$$z_{depth} = -P_{min}\left(T_{z,t+\Delta t} \geq T_F\right)\Delta d \tag{13}$$

where $T_{y,z,t+\Delta t}$ is the temperature distribution in the y-z section at the time, $T_{z,t+\Delta t}$ is temperature distribution along the centre line of the y-z section. z_{depth} is the maximum depth of the material failure layer, T_F is the material failure temperature, and P_{min} is the minimum position for

the temperature on the centre line of the y-z section over the failure temperature.

The laser beam parameters used here are from a continuous-wave carbon dioxide generator (LE900, Hongfan Tech. Company) with a maximum power of 60 W, a wavelength of 10.6 μm, and a circular focus with a diameter of 0.3 mm, and a focal length of 12.5 mm.

2.2. Material properties

A standard commercial resin bond diamond grinding wheel (D125N75B771/8, 3M Company, see more details in Table 1) was employed in this study for its wide applications, good self-sharpening ability and low risk of grinding burn.

As the grinding wheel is a multi-material-based tool, to study the overall properties of the grinding wheel materials, each of the main ingredients is investigated first, including the exact content and properties. As shown in Fig. 3(a), the main ingredients for this kind of wheel include grits, resin bond, and pores. However, pores are not practically achievable for the resin bond grinding wheel, and additives often instead of pores are added to the bond [32]. The other two or more ingredients' contents usually remain confidential for commercial purposes.

To determine the exact ingredient contents of the grinding wheel, Energy Dispersive Spectrometer (EDS) (174C CZ, ZEISS Company) detecting technology was employed (see Fig. 3b). The results revealed the weight and volume percentage of each content of the grinding wheel. It indicated that the main additive was copper, which accounts for 16.19 % ± 2 % of the whole material in weight percentage (see Fig. 3c) and around 3.83 % in volume percentage (see Fig. 3d).

According to ingredients, the samples were well prepared and tested by the HyperFlash (LFA 467, NETZSCH) in the Ningbo Institute of Materials Technology & Engineering, CAS. The details of the material properties of the employed diamond grinding wheel are shown in Table 2.

2.3. Flowchart

The flowchart concluding the modelling steps for the full calculation is presented in Fig. 4. All the equations mentioned above were transferred into codes in MATLAB. The input parameters include laser power and feed rate, while the output results include temperature field distribution and ablation depth. Eq. (10) was first used to calculate the laser intensity, and then Eqs. (8) & (9) were employed to compute the energy absorbed by the workpiece, the temperature field distribution and ablation depth can finally be solved by Eq. (1)–(3) and Eq. (11)–(13).

The time step for the stability of this calculation is governed by the Biot and Fourier number in the following way for problems in a numerical format [27]:

$$B_i = \frac{h_n \Delta d}{k} \tag{14}$$

$$F_o = \frac{k\Delta t}{\rho C_\rho (\Delta d)^2} \tag{15}$$

where the stability requirement for the interior node is $F_o \leq \frac{1}{4}$, for the convection boundary node is $F_o(2 + B_i) \leq \frac{1}{2}$, and for the exterior corner with a convection boundary is $F_o(1 + B_i) \leq \frac{1}{4}$.

As can be seen, Δt and Δd are the only two changeable parameters in the function that decided the two stability factors. Values for Δd (0.01 mm) are firstly selected according to the measurement precision that the experimental setup is able to achieve. By fixing the cells' edge length Δd, the basic time step Δt requirement for simulation stability can be calculated. To further improve the simulation precision and understand the details in the process, the time step was reduced until it had little effect on the simulation results. From this process, a time step of 10^{-4} s was finally selected.

Table 1
The details of the used diamond abrasive grinding wheels in the simulation.

Shape	Size (mm)	Abrasive type	Grit no. (#)	Hardness	Concentration (vol%)	Bond
Plate	Φ125 × Φ32 × 20	Diamond	120	N	75	Resin

3. Simulation results and analysis

3.1. Temperature field response with time

Fig. 5 shows the cross-sectional view of the temperature field response with time (within the first 2 s) during the laser ablation process under laser power of 24 W and a feed rate of 3.0 mm/s. Specifically, Fig. 5(a) shows the transient temperature distribution along the cross-section of the slot for times of 0 s, 0.5 s, 1.0 s, 1.5 s and 2.0 s. It indicated that the most significant temperature field changes happened in the first 0.5 s, while it remained nearly unchanged for the time from 1.0 s to 2.0 s.

As the most significant temperature field changes happened in the first 0.5 s, smaller time intervals were used to present the simulation results. Fig. 5(b) and (c) show the temperature distribution along the cross-section for the time from 0.01 s to 0.1 s, with an interval of 0.01 s. It revealed that the temperature field extended in both directions within a short time. However, the temperature gradient of isotherms in width direction is much denser than depth direction, which indicated the temperature spreads faster along depth direction. Probably, it was because of the directivity of a laser beam that made heat flow largely along the laser beam propagation direction. While the time period was tiny, little heat was absorbed by the workpiece and transferred within the ablation zone.

Given that the trend of the temperature field is stabilising during the time from 0.01 s to 0.1 s, a slightly larger time interval of 0.1 s is employed to present the results from the time at 0.1 s to 1.0 s, as shown in Fig. 5(d) and (e). As more heat flows into the ablation zone with time, it showed that the temperature field started to expand in both the width and depth directions during the time from 0.1 s to 0.5 s, as shown in Fig. 5(d). However, it is worth noting that the temperature field stopped extending along the depth direction and mainly extended along the width direction for the time from 0.6 s to 1.0 s, as shown in Fig. 5(e). Three reasons might account for this phenomenon: (i) the laser beam energy cannot flow deeper with the laser defocusing effect and the absorption of energy by surrounding materials, (ii) the moving of the laser beam makes the energy flow into different positions of the workpiece, and (iii) the heat balance in the ablation zone makes the processing enter a stable processing stage.

3.1.1. Temperature field response to ablation parameters

As demonstrated, the temperature field remains nearly unchanged after 1.0 s (as shown in Fig. 5), the following section considers the simulation at 2.0 s as the stable stage. The simulation results of temperature field distribution for lateral section and cross-section under the feed rates of 3.0 mm/s, 4.0 mm/s, 5.0 mm/s, and 6.0 mm/s with different laser powers (from 24 W to 60 W with an interval of 24 W) are shown in Fig. 6. The temperature field variation with feed rate under a specific laser power was recorded in each sub-chart. Overall, it showed that the shapes of the temperature field distribution were unchanged under a specific feed rate, but the core temperature of the temperature field increased with the laser power.

Fig. 6(a & b) shows the temperature fields change with feed rate under the laser power of 24 W. They indicated the lateral sections of the

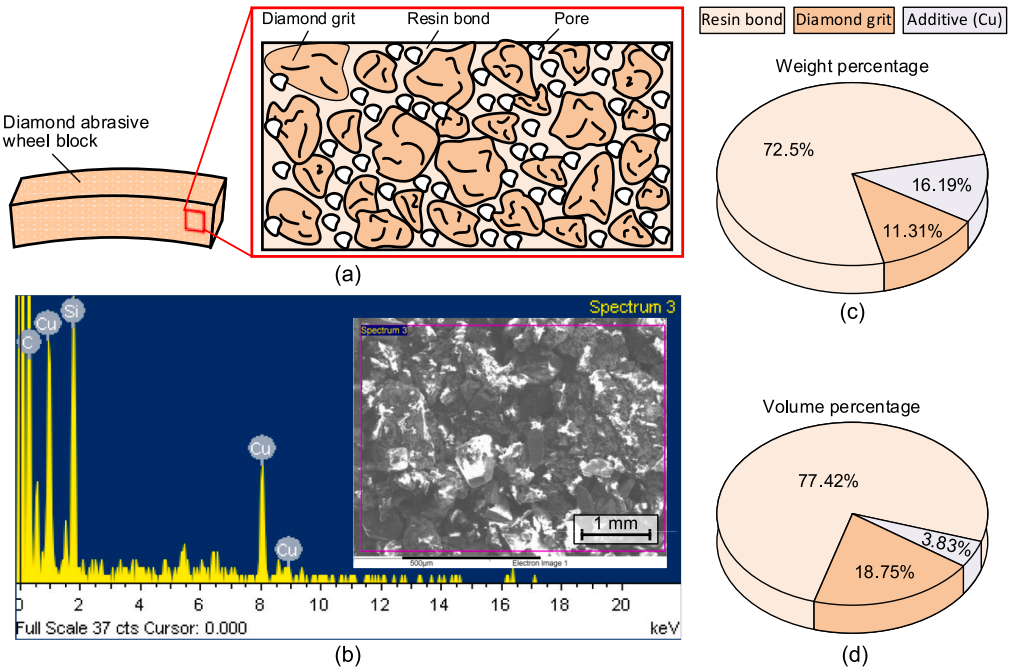

Fig. 3. The ingredients and percentages of the diamond abrasive wheel. (a) The grinding wheel block and ingredients; (b) the EDS detection results for ingredients' elements; (c) the weight percentage and (c) volume percentage determination in the grinding wheel.

Table 2
Material properties.

Properties (symbol)	Value	Units
Absorptivity (A_b)	0.85	N/A
Latent heat of fusion (L_f)	260	kJ/g
Material failure temperature (T_f)	650	K
Specific heat capacity (c)	0.839	J/(g·K)
Density (ρ)	2.783	g/cm^3
Thermal conductivity rate (λ)	3.717	W/(m·K)
Thermal diffusivity (α)	1.592	mm^2/s

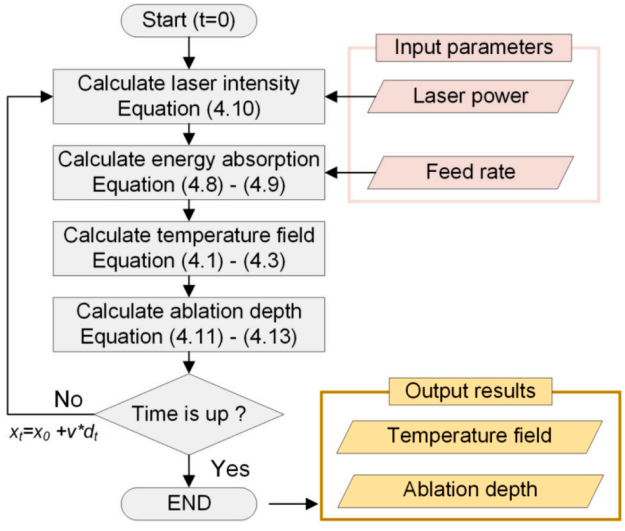

Fig. 4. Flowchart for the theoretical model, solving the temperature field distribution and ablation depth estimation by inputting processing parameters of laser power and feed rate.

temperature field boundaries were increased with the feed rate, while the cross-sections of them were reduced. In addition, the core temperatures for the temperature field dropped slightly with the feed rate. This phenomenon was because less heat flowed in the core with increasing feed rate, and the influent heat had limited time to spread around. The other sub-diagrams (as shown in Fig. 6) showed a similar trend, but the higher core temperature field kept increasing as the laser power increased. Compared to the results from the laser power of 24 W, the highest core temperature was raised from 900 K to 1500 K. There was no doubt that more heat would flow into the ablation zone when the laser power increased, resulting in the temperature increase in the ablation zone.

It is worth noting that, although the core temperature of the heat-affected cross-section kept increasing with the laser power, the temperature field widths were not dramatically increased (e.g., all the cross-section widths tend to be 3.90 mm under 3 mm/s with laser powers from 24 W to 60 W). Besides, it showed a clear drop in the width of the temperature field with the increase in feed rate (e.g., the cross-section width dropped from 3.90 mm to 2.35 mm when the feed rate increased from 3 mm/s to 6 mm/s under the laser power 24 W). This phenomenon indicated that the increased laser power would not dramatically broaden the heat-affected zone, but the rising feed rate would clearly narrow the heat-affected site. Meanwhile, the expanded temperature field distribution along the lateral section with feed rate indicated the ablation efficiency could be improved by the increased feed rate.

When comparing the simulation results from Fig. 6(b, d, f, h), it revealed that the shapes of the temperature field distribution under different laser powers were almost the same. However, differently, the core temperature increased with the laser power, rising from around 800 K at 24 W to about 1500 K at 60 W. In all, the presented figures showed that the increased feed rates would decrease the heat-affected zone. These phenomena may largely be due to the increased heat source passing speed leaving little time for the heat to flow around. Meanwhile, a good match of the feed rate and the increased laser power would not largely affect the heat-affected area, but it would be beneficial to material removal. The fierce laser power could induce the target material removal in no time and a proper feed rate could make the heat

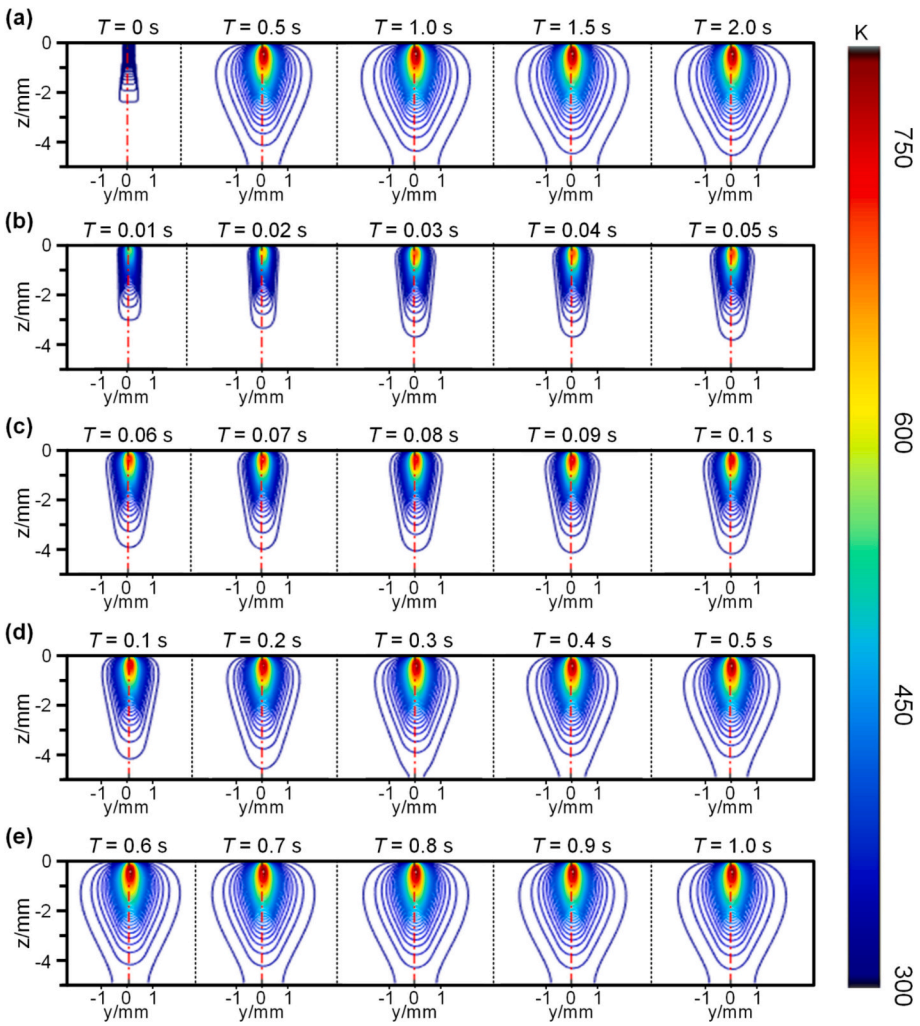

Fig. 5. Temperature field responses to time during laser ablation under the laser power of 24 W and feed rate of 3 mm/s. The transient temperature field of the slot cross section for (a) the time at 0 s, 0.5 s, 1.0 s, 1.5 s and 2.0 s, (b) the time at 0.01 s, 0.02 s, 0.03 s, 0.04 s and 0.05 s, (c) the time at 0.06 s, 0.07 s, 0.08 s, 0.09 s and 0.1 s, (d) the time at 0.1 s, 0.2 s, 0.3 s, 0.4 s and 0.5 s, and (e) the time at 0.6 s, 0.7 s, 0.8 s, 0.9 s and 1.0 s.

source move to the new area quickly before there's a huge influx of heat.

In conclusion, the results showed that the shapes of the temperature field distributions for a specific feed rate do not change significantly. However, the core temperature for the temperature field increased with the laser power. Besides, as the temperature field distribution for a specific feed rate do not change significantly, the increased laser power would not significantly enlarge the heat-affected zone. Therefore, the results indicated that a higher processing efficiency could be achieved by increasing the laser power.

3.1.2. Ablation depth responses to ablation parameters

Although it was reported that the actual working temperature of the resin-bonded diamond grinding wheel should not exceed 533 K [33], or it would be damaged, we found from our previous studies that the damage to the grinding wheel was a gradual process because of the natural characteristics of organic materials [12]. The actual temperature that could lead to obvious damage to the grinding wheel in a short time via the CO_2 laser was above 650 K [12]. Therefore, 650 K was set as the threshold for the laser ablation depth simulation. Based on this crucial temperature, the simulation results of ablated depths, areas and fluctuations under the feed rate of 3.0 mm/s, 4.0 mm/s, 5.0 mm/s, and 6.0 mm/s with laser power from 24 W to 60 W with an interval of 12 W are presented in Fig. 7.

Generally, it showed the ablation depth decreased with the feed rate and increased with the laser power. Specifically, the minimum ablation depth of the figure was −0.83 mm at 24 W with a feed rate of 6.0 mm/s while the maximum ablation depth reached −2.33 mm at 60 W with a feed rate of 3.0 mm/s. The ablation depth dropped by 0.29 mm as the feed rate doubled (from −1.12 mm at 3.0 mm/s to −0.83 mm at 6.0 mm/s) when the laser power was 24 W (see Fig. 7a). With the laser power increasing, this figure kept rising from 0.32 mm at 36 W (see Fig. 7b), via 0.35 mm at 48 W (see Fig. 7c), to 0.41 mm at 60 W (see Fig. 7d). These data indicated that the effect of feed rate on ablation depth increased when the power was higher. This may be attributed to the high laser power providing more energy to the ablation zone, while the variation of feed rate caused the energy to interact with the ablation zone more violently.

To be more clearly, Fig. 8 shows the feed rates effect on the simulation results under various of laser powers. It showed that apart from the reduced ablation depth as the feed rate increased (see Fig. 8a), the most noticeable change was that the ablation depth tended to be early to enter the stable stage (see Fig. 8b). It can be noted that the fluctuations stopped within 0.6 s on average when the ablation processes were started. Nevertheless, the fluctuation can be suppressed within 0.2 s when the feed rate was 6.0 mm/s at laser powers from 24 W to 60 W. This may be because a fast-feeding laser spot made the laser power transfer less heat to the ablation zone, and the material removal due to thermal shock was more dominant than thermal build-up.

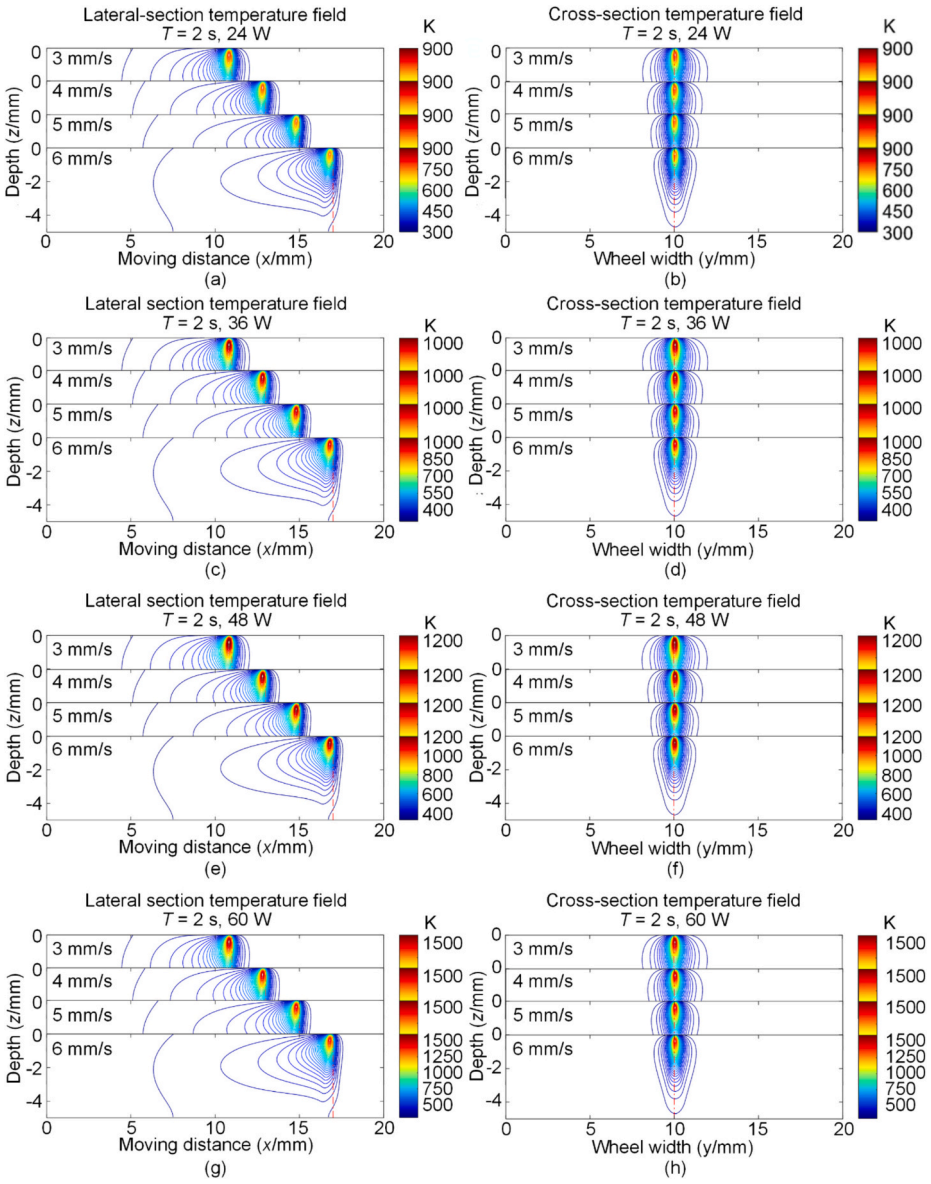

Fig. 6. Simulation results of temperature field distribution response to feed rates from 3.0 to 6.0 mm/s with an interval of 1.0 mm/s under the laser power from 24 to 60 W with an interval of 12 W. (a), (c), (e) and (g) are the lateral section view (from x-z plane) and (b), (d), (f) and (h) are the cross-section view (from y-z plane) for the laser power of 24 W, 36 W, 48 W and 60 W, respectively.

More interestingly, the figures showed that the ablation depth decreased with the increased feed rate for specific laser power, but the decline rates relative to the ablation depth were tiny (maximum 0.41 mm relative to the depth range 1.92 mm - 2.33 mm, see Fig. 7d). As a result, the ablated lateral areas (the laser moved distance multiplied by the ablation depth) were increased with the feed rate (see Fig. 8a). More specifically, these areas increased from 6.72 mm^2 to 9.96 mm^2 as the laser power increased from 3 mm/s to 6 mm/s when the laser power was 24 W, increased by 3.24 mm^2. This figure kept increasing as laser power enhanced. When it came to 60 W, these areas rose by 6.30 mm^2, almost double that at 24 W. These results indicated that the machining efficiency could be improved by raising the feed rate and laser power. Meanwhile, as the material removal rate should be a constant for fixed laser power, the cross sections of the ablated zones were sure to be narrowed with the feed rate increasing. The narrowed cross sections mean less heat effect zone. These phenomena therefore suggested that increasing the feed rate in conjunction with a higher laser power should improve machining efficiency and reduce heat-affected zones.

In summary, Figs. 7 and 8 show that the tendencies under different laser powers are consistent in that the ablation depth dropped with the feed rate under a certain laser power and increased with the laser power for a fixed feed rate. The ablation depth increased with the laser power under each feed rate and the ablation depth kept an increasing trend with an increased laser power. Moreover, it took about 1.0 mm transition distance (in the x-direction) to reach the relatively stable position. As the feed rate increased, the depth fluctuation can be quickly suppressed. Meanwhile, with the feed rates increased under a definite laser power, the ablated areas were enlarged, and the section cross was narrowed, which indicated that a steeper ablation edge could be achieved by increasing the laser power. Finally, it can be seen that a good match of feed rate with a higher laser power can be employed for various purposes.

4. Experimental study

4.1. Experimental methodology

Since this paper aims to study the effects of laser parameters on the

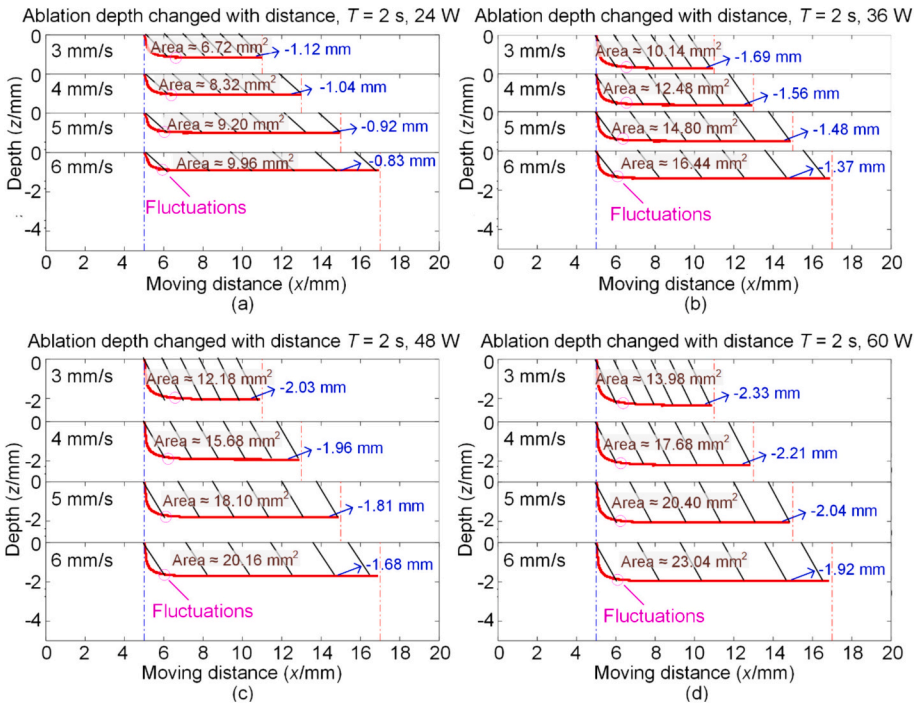

Fig. 7. Simulation results of the ablation depth response to feed rate from 3.0 mm/s to 6.0 mm/s with an interval of 1.0 mm/s under the laser power from 24 W to 60 W with an interval of 12 W. (a), (b), (c) and (d) are the ablation depth for the laser power of 24 W, 36 W, 48 W and 60 W, respectively.

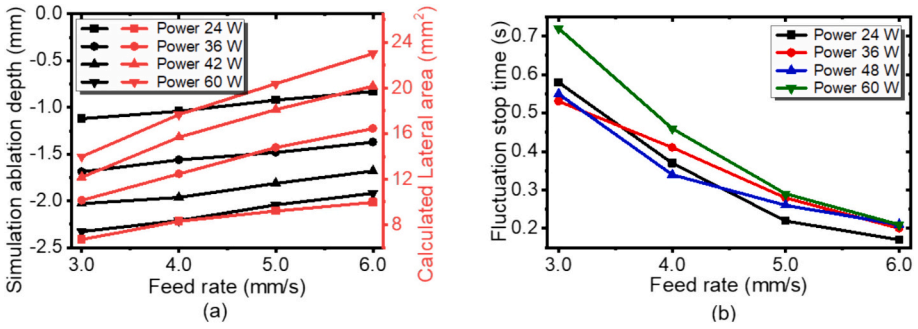

Fig. 8. Feed rates effect on the simulation results under various of laser powers. (a) Effects on ablation depth and lateral area. (b) Effects on fluctuation stop time.

ablated surface topography, wide ranges of both laser power and feed rate were employed. To make all the results comparable, all the laser ablation trials, using seven laser powers and eight laser feed rates, were produced on a single diamond wheel surface in air. Fig. 9 gives an overview of the experimental methodology. As seen in Fig. 9(a), the whole wheel was divided equally into eight segments (see segments A to H) along the wheel circumferential direction and in each segment there were seven ablated tracks along the wheel axis direction (see track X1 to X7 where X refers to A-H). The laser feed rate was increased incrementally by 1.0 mm/s from the segment A to H, while the laser power was incrementally increased at an interval of 6 W from the track X1 to X7 (where X refers to A-H). The experimental parameters are detailed in Table 3.

Standard commercial diamond abrasive grinding wheels (D120N75B771/8, 3M Company) were used in all the trials in this study (see more details in Table 1). The laser beam was generated by a continuous-wave carbon dioxide generator (LE900, Hongfan Tech. Company) with a maximum power of 60 W, a wavelength of 10.6 μm, a circular focus with a diameter of 0.3 mm, and a focal length of 12.5 mm. The linear and angular motions and positions of the ablated diamond wheels were accurately controlled using a specially made positioning system, having translational and rotational motion accuracies of 10 μm and 0.05° based on the G-code-based SIEMENS NC system.

As seen in Fig. 9(b), the positioning system consisted of: a controller (BR010-11T8X2M, BenT CNC Automation Equipment Company), driver (ZD-M42, Philips Company), stepper motor (42HS4013A4CE, Sumtor Company), reducer (SK4248-19.2, Yixing Technology Company) and other auxiliary hardware, enabling 2-axis simultaneous motions (which were the translational and the rotational motions separately along and around the wheel axis). The translational and rotational motion speeds were controlled separately within the ranges of 0–100 mm/s and 0–15°/s.

After the laser ablation, the diamond wheel was firstly carefully cut into eight segments (A-H) by the handsaw and wire-EDM machine (MV2400S, Mitsubishi Electric Company), as shown in Fig. 9(c) and (d). The two cross sections of each segment were carefully ground and polished by the alumina with the sizes of #600 (2 h), #1200 (2 h), and #2000 (2 h). Each segment then was cleaned by the ultrasonic distilled water bath for 1 h and air-dried at room temperature, as shown in Fig. 9 (e) and (f). Various analyses based on Scanning Electron Microscope

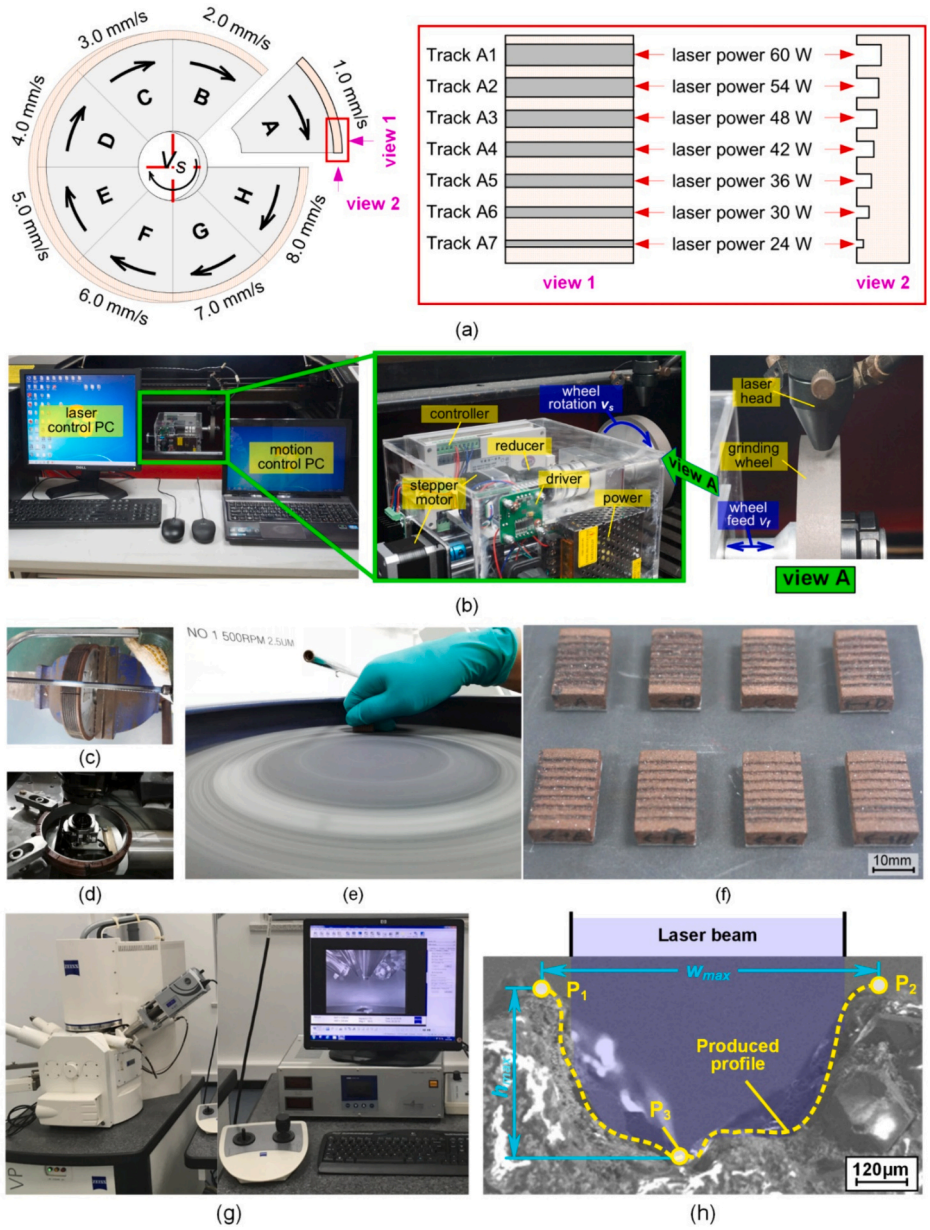

Fig. 9. Experimental methodology. (a) Ablation strategy, where the whole wheel was equally divided into eight segments (see segments A to H) along the wheel circumferential direction and in each segment, there were seven ablated tracks along the wheel axis direction (see track X1 to X7 where X refers to A-H). The laser feed rate was incrementally increased from the segment A to H, while the laser power was incrementally increased from the track X1 to X7 (where X refers to A-H); (b) experimental setup containing control system (left), positioning system (middle) and the detailed position view (right); (c) cutting through the abrasive layer of samples via hand saw and (d) cutting off the sample from the grinding wheel via EDM, (e) polishing both sides of the samples and (f) drying them at the room temperature; (g) observation of the ablated slots via SEM and (h) the measurement of the results by three key points.

Table 3
Laser parameters employed in the trials.

Trial No.	Laser power (W)	Laser feed rate (mm/s)	Segment no.	Track no. in each segment	Trial no.	Laser power (W)	Laser feed rate (mm/s)	Segment no.	Track no. in each segment
1–7	60,54,	1.0	A	A1-A7	29–35	60,54,	5.0	E	E1-E7
8–14	48,42,	2.0	B	B1-B7	36–42	48,42,	6.0	F	F1-F7
15–21	36,30,	3.0	C	C1-C7	43–49	36,30,	7.0	G	G1-G7
22–28	24	4.0	D	D1-D7	50–56	24	8.0	H	H1-H7

(SEM) (174C CZ, ZEISS Company) were performed to observe and measure the ablated topographies respectively, the ablated structure topography was evaluated based on the three key points on the observed cross-section profiles, as seen in Fig. 9(g) and (h).

4.2. Experimental results and analysis

Fig. 10 shows the comparisons of the section view for experimental SEM and the simulation images of the laser-ablated topography under

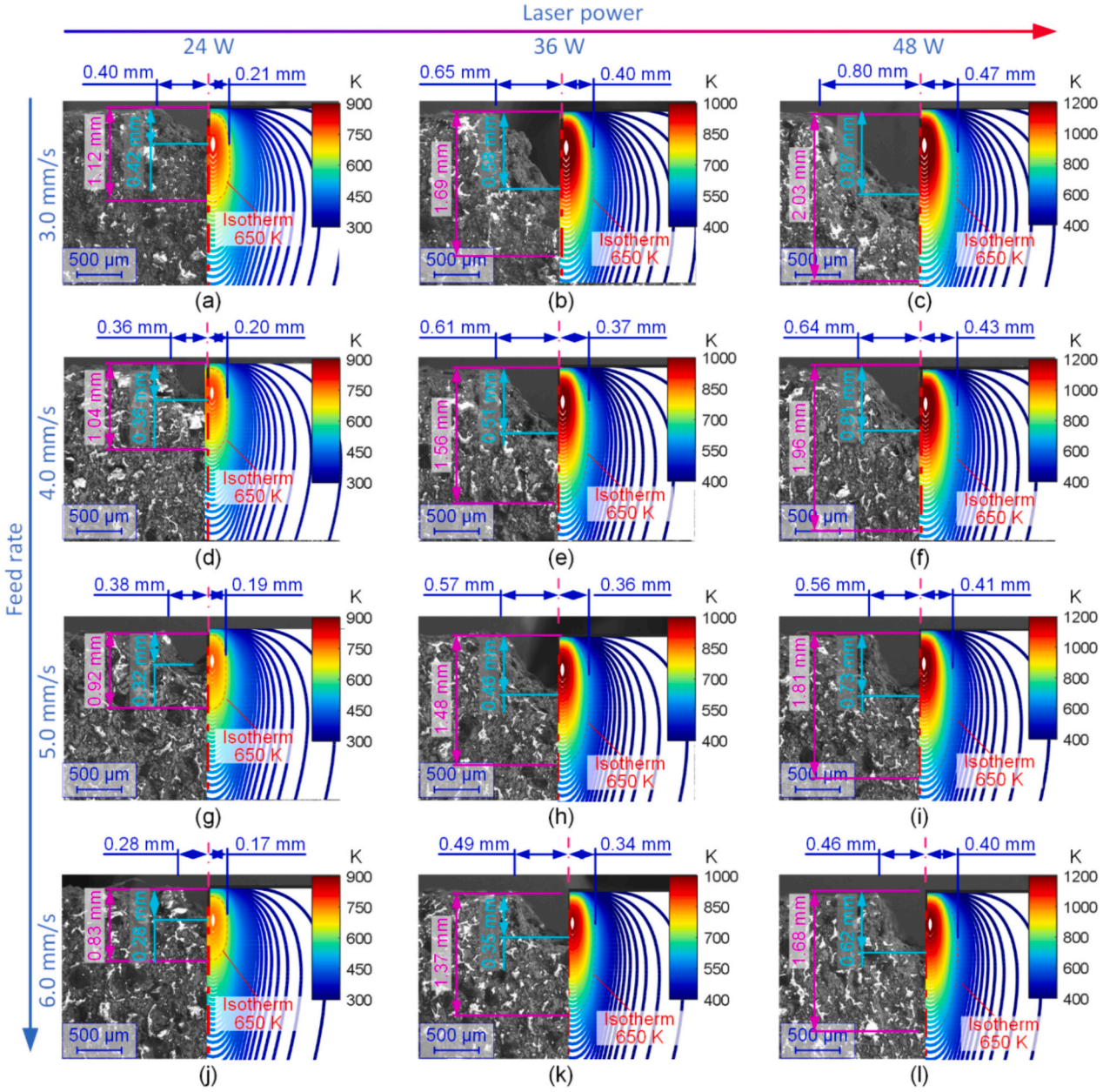

Fig. 10. Comparisons of the section view for experimental SEM and the simulation images of the laser-ablated topography under different processing parameters. The ablation result from the feed rate of (a) 3.0 mm/s, (d) 4.0 mm/s, (g) 5.0 mm/s and (j) 6.0 mm/s under the laser powers of 24 W; (b) the ablation result from the feed rate of (b) 3.0 mm/s, (e) 4.0 mm/s, (h) 5.0 mm/s and (k) 6.0 mm/s under the laser powers of 36 W; the ablation result from the feed rate of (c) 3.0 mm/s, (f) 4.0 mm/s, (i) 5.0 mm/s and (l) 6.0 mm/s under the laser powers of 48 W.

different processing parameters. Generally, the trends in the experimental results were consistent with that in the simulation where the trenches' profiles of the section areas were increased with the laser power and decreased with the feed rate. However, some inconsistencies were found between the ablated profiles and depths against the temperature fields distribution in the simulation due to (i) the organic nature of the resin bond that there is no fixed failure temperature and (ii) the complex physical properties of the mixed multiple materials within the resin bond diamond grinding wheels. Nevertheless, the trends and the temperature field distributions gained from the simulation results were valuable in guiding the experimental scheme design and predicting experimental results, which was significant in both academic study and industrial production.

Specifically, both the experimental and simulation results showed the section profiles of the ablated trenches were increased with the laser power and decreased with the feed rate. To be different, the ablation depths achieved from the simulation were much bigger than those from the experiments. For the laser power of 48 W, the ablation depths obtained from the simulation were more than 2 times that from the trials and the figures for the laser power of 24 W and 36 W were almost 3 times. As an idealised model employed in the simulation, the results were not able to consider the failure characteristics of organic materials. That means the materials may not fail at the crucial temperature unless they are exposed for a certain time. Besides, given the mass of heat lost as the materials are removed from the ablation zone, the actual temperature in the ablation zone should be lower than the simulation. Therefore, the ablation depths in the experiments were much smaller than in the simulations.

Surprisingly, when it came to the ablation width, it showed the ablation width achieved from the simulation was smaller than the

experiments. It may be due to the factors that were not considered in the model, like (i) mass of heat was brought to the surface layer due to thermal convection phenomenon as gases/materials in the ablation zone melt, boil, evaporation, and expansion; (ii) the heat combined with the borderline effect made the edges of the ablated trenches easily damaged in experiments. However, it is interesting that the differences were reduced when the feed rate increased and the width tends to the diameter of the laser beam (see the differences between Fig. 10a, b & c and j, k & l). This may be because of the fast movement of the laser beam, making the heat less likely to be accumulated and transferred around.

To be clearer, Fig. 11 presents the comparison of ablation depth and width between experimental and simulation results shown in Fig. 10. Specifically, Fig. 11(a) shows that the simulation ablation depths were closely correlated to the experimental. With the increases in the feed rate, both the simulation and experiment results showed the ablation depths dropped nearly linearly. The ablation depth range of the simulation results for the processing parameters was from 0.83 mm to 2.03 mm, while this figure for the experimental was from 0.28 mm to 0.87 mm. Meanwhile, Fig. 11(b) showed a relatively complex figure that the ablation width nearly remained unchanged when the laser power was 24 W in both simulations and experiments. As the laser power increased, the ablation width change tended to be limited in the experiment and the tendency for the simulation also became gentle. It indicated the ablation width would vary in a limited space eventually despite the increase of laser power. As for the significant overlap of error bars, this may be because the resin-bonded grinding wheel contains convex abrasive and concave porous. As these microstructures are affected by the random grits and pores distribution, significant fluctuations are inevitably avoided.

To better comprehend the implications of this study, two evaluation indices were defined, as depicted in Fig. 12: (i) the W_T/D_L ratio and (ii) the H_T/W_T ratio. Here, W_T represents the width of the ablated trench, D_L is the focal diameter of the laser beam and H_T signifies the depth of the ablation trench. The W_T/D_L ratio was established to assess the heat-affected zone. This is because the materials eliminated beyond the laser spot range were not directly influenced by laser, but rather due to the effects of heat transfer. Consequently, a lower ratio indicates a smaller heat-affected zone. On the other hand, the H_T/W_T ratio was designed to evaluate the quality of the ablation. This ratio reflects whether the target materials were primarily removed along the direction of laser propagation, and subsequently, whether the removed target materials were controlled and precise. Therefore, a higher the aspect ratio corresponds the superior ablation quality.

The SEM images showed the heat-affected zone increased rapidly with the laser power at a low feed rate (see Fig. 12a & b), but it increased little at a high feed rate (see Fig. 12c & d). Therefore, a low feed rate was quite unfavourable for suppressing the heat-affected zone. To quantify the effect, Fig. 12(e) & (f) showed comparisons of HAZ and aspect ratio changes with feed rates under different laser powers. It indicated the HAZ decreased with the laser power dropping and the feed rate increasing, but the effect of laser power on HAZ gradually became tiny as the feed rate increased (see Fig. 12e). Besides, it showed the aspect ratio increased with the laser power and the feed rate. Interestingly, the feed rate was also affected more than the laser power, as there was a crossover in the changes for the aspect ratio when the laser powers were 36 W and 48 W (see Fig. 12f).

In summary, both indices reveal that the ablation quality was improved when the feed rate increased under a matched laser power, which was consistent with the simulation results. Some leading industrial companies have noticed this issue through trial and error while they cannot explain it from the theoretical aspect. In response, they keep increasing the laser power and feed rate, e.g., Han's laser has increased its laser power from 2000 W to 12,000 W and feed rate from 1200 mm/s to 2300 mm/s in the past five years [34]. Undoubtedly, the work in this paper provides significance to both the theoretical study and industrial production.

5. Conclusions

To better understand the laser ablation process on resin-bond diamond grinding wheels, a mathematical model was established to study the unsteady-state conduction in the composite. The time-dependent temperature distribution with the laser power and feed rate within the heat-affected zone was revealed. The ablation depth change along the feed direction was calculated. Finally, experimental work was performed to validate the simulation results and demonstrate the usefulness of the study. The key conclusions could be summarised as follows:

(1) By using the finite element difference method, a mathematical model considering the focused laser spot size, the laser beam energy intensity distribution along with propagation direction, and the heat conduction and convection in the ablation process was established. Both the time-dependent temperature distribution in the heat-affected zone and ablation depth could be predicted by this model.
(2) The simulation results showed that the laser power minimally impacted the shape of temperature field distribution, but it improved the core temperature of the ablation zone as the laser power increased. Meanwhile, the temperature field shrank as the feed rate increased. According to the dynamic temperature field distribution from the simulation model, the section topography of the ablated slot can be generally predicted. Besides, the heat-affected zone range can also be estimated using the model.
(3) The experiment showed the trends of the results were generally consistent with the simulation. However, significant differences were also found regarding the specific values as the model obtained the topography by calculating critical temperature and was unable to take the factors, e.g., borderline effect, heat transfer by melting, and evaporation, into consideration. To a certain extent, the simulation results were experimentally proved.

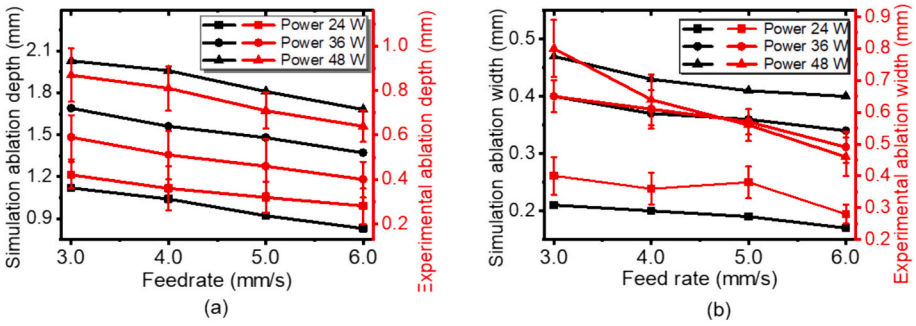

Fig. 11. Comparison of experimental and simulation results. (a) Ablation depth and (b) ablation width of the results.

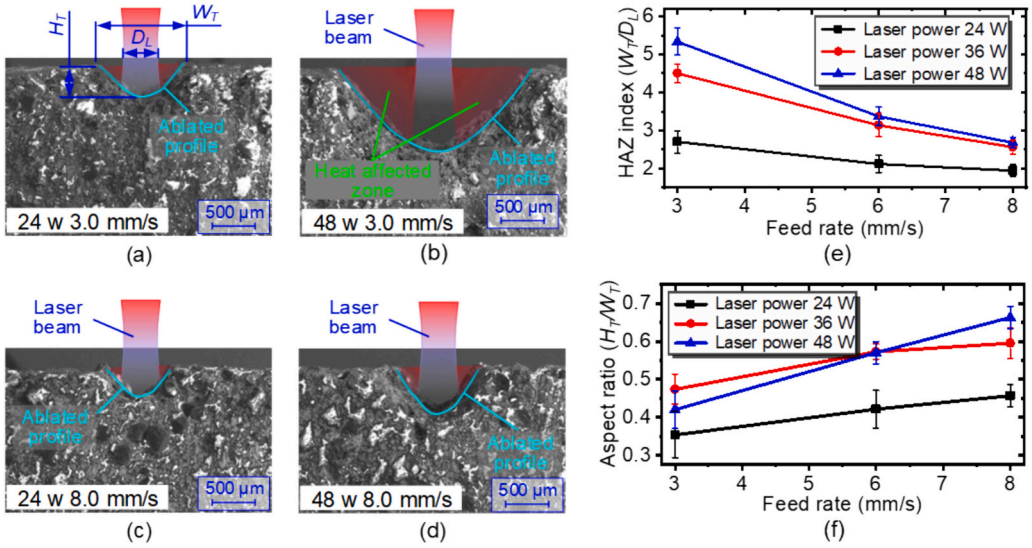

Fig. 12. The SEM images of the ablated profile under different processing parameters and the definition of evaluation indexes. The SEM image comparisons of (a) 24 W and (b) 48 W under the feed rate of 3.0 mm/s. The SEM image comparisons of (c) 24 W and (d) 48 W under the feed rate of 8.0 mm/s. (e) The heat-affected zone index (W_T/D_L) and (f) aspect ratio (H_T/W_T) change with feed rate under different laser power.

Based on the conclusions drawn from the study, the general ablation laws could be determined. Potentially, the results from the study could be used to reduce the heat-affected zone, generate the desired profile, and improve efficiency and accuracy, which was of great significance to both industrial production and academic studies.

Author agreement

We the undersigned declare that this manuscript entitled "On the Modelling and Experimental Study of CO_2 Laser Ablation on Resin-bond Diamond Grinding Wheels: Understanding the Effect of Processing Parameters on the Time-dependent Temperature Field" to be considered for publication in Journal of Manufacturing Processes is original, has not been published before and is not currently being considered for publication elsewhere.

We would like to draw the attention of the Editor to the following publications of one or more of us that refer to aspects of the manuscript presently being submitted. Where relevant copies of such publications are attached.

We confirm that the manuscript has been read and approved by all named authors and that there are no other persons who satisfied the criteria for authorship but are not listed. We further confirm that the order of authors listed in the manuscript has been approved by all of us.

We understand that the Corresponding Author is the sole contact for the Editorial process. He is responsible for communicating with the other authors about progress, submissions of revisions and final approval of proofs.

Signed by all authors as follows: Ke Ge Xie; Adam Rushworth; Hao Chen; Jin Yi Li.

CRediT authorship contribution statement

Ke Ge Xie: Writing – review & editing, Writing – original draft, Methodology, Investigation, Formal analysis, Data curation, Conceptualization. **Adam George Antrum Rushworth:** Writing – review & editing, Supervision, Resources, Funding acquisition, Conceptualization. **Hao Chen:** Writing – review & editing, Supervision, Conceptualization. **Jinyi Li:** Writing – review & editing, Software, Investigation.

Declaration of competing interest

The authors declare that they have no known competing financial interests or personal relationships that could have appeared to influence the work reported in this paper.

Data availability

Data will be made available on request.

Acknowledgements

The authors acknowledge the support of the National Natural Science Foundation of China (NSFC) [grant number 52035009] and the University of Nottingham, Ningbo, China [grant number I01180800099, I01190100001]. Additionally, the authors appreciate the supervision of Prof. Dragos Axinte (University of Nottingham, United Kingdom) and Prof. Hui Deng (Southern University of Science and Technology), and thank Prof. Haonan Li (University of Nottingham, Ningbo, China) who started the project with the authors.

References

[1] Du ZJ, Zhang FL, Xu QS, Huang YJ, Li MC, Huang HP, et al. Selective laser sintering and grinding performance of resin bond diamond grinding wheels with arrayed internal cooling holes. Ceram Int 2019;45:20873–81. https://doi.org/10.1016/j.ceramint.2019.07.076.
[2] Li MC, Zhang FL, Zhou YM, Li WX, Wu SX, Wu SH. Preparation and performance of resin-bonded grinding wheel with braze-coated diamond grits. Diamond Relat Mater 2020;101:107619. https://doi.org/10.1016/j.diamond.2019.107619.
[3] Yin L, Huang H. Ceramic response to high speed grinding. Mach Sci Technol 2004;8:21–37. https://doi.org/10.1081/MST-120034240.
[4] Dai L, Chen G, Li M, Yuan S. Efficient and precision dressing of arc-shaped diamond grinding wheel by laser dressing and electrical discharge dressing. Diamond Relat Mater 2022;125:108978. https://doi.org/10.1016/j.diamond.2022.108978.
[5] Deng H, Xu Z. Laser-dressing topography and quality of resin-bonded diamond grinding wheels. Opt Lasers Eng 2021;136:106322. https://doi.org/10.1016/j.optlaseng.2020.106322.
[6] Yang Z, Zhang S, Zhang Z, Zhang Y, Hu J, Li K, et al. Experimental research on laser-ultrasonic vibration synergic dressing of diamond wheel. J Mater Process Technol 2019;269:182–9. https://doi.org/10.1016/j.jmatprotec.2019.01.031.
[7] Cha D, Axinte D. Transient thermal model of nanosecond pulsed laser ablation: effect of heat accumulation during processing of semi-transparent ceramics. Int J Heat Mass Tran 2021;173:121227. https://doi.org/10.1016/j.ijheatmasstransfer.2021.121227.

[8] Walter C, Komischke T, Kuster F, Wegener K. Laser-structured grinding tools - generation of prototype patterns and performance evaluation. J Mater Process Technol 2014;214:951–61. https://doi.org/10.1016/j.jmatprotec.2013.11.015.
[9] Rabiey M. Dry grinding with CBN wheels, the effect of structuring. University of Stuttgart; 2011.
[10] Zhang R, Huang CZ, Wang J, Feng SC, Zhu HT. Evolution of micro/nano-structural arrays on crystalline silicon carbide by femtosecond laser ablation. Mater Sci Semicond Process 2021;121:105299. https://doi.org/10.1016/j.mssp.2020.105299.
[11] Cai JW, Pan XT, Yuan HC, Zhang YF, Meng F, Zhang MF. Experimental study of diamond ablation based on femtosecond laser. Optik 2020;217:164838. https://doi.org/10.1016/j.ijleo.2020.164838.
[12] Li HN, Xie KG, Wu B, Zhu WQ. Generation of textured diamond abrasive tools by continuous-wave CO2 laser: Laser parameter effects and optimisation. J Mater Process Technol 2020;275:116279. https://doi.org/10.1016/j.jmatprotec.2019.116279.
[13] Xie KG, Rushworth A, Chen H, Zhang XY, Huang ZP, Shen YX. Generating precise non-flat grinding wheel surfaces via CO2 laser ablation: understanding the relationship between overlap rate and feed rate on composite materials. J Manuf Process 2022;83:339–53. https://doi.org/10.1016/j.jmapro.2022.09.008.
[14] Rushworth A, Xie KG, Fang BL, Shen YX, Huang ZP, Zhang XY. Generating profiled diamond grinding wheels by 2000 W fiber laser: on the understanding of laser ablation law with high power and establishment of a predictive model. Int J Adv Manuf Technol 2022;120:3045–63. https://doi.org/10.1007/s00170-022-08934-6.
[15] Butler-Smith PW, Axinte D, Daine M. Preferentially oriented diamond micro-arrays: a laser patterning technique and preliminary evaluation of their cutting forces and wear characteristics. Int J Mach Tool Manuf 2009;49:1175–84. https://doi.org/10.1016/j.ijmachtools.2009.08.007.
[16] Parthiban A, Dhanasekaran C, Sivaganesan S, Sathish S. Modeling on surface cut quality of CO2 laser cutting for austenitic stainless steel sheet. Mater Today-Proc 2020;21:823–7. https://doi.org/10.1016/j.matpr.2019.07.428.
[17] Ge Q, Gu DD, Dai DH, Ma CL, Sun YX, Shi XY, et al. Mechanisms of laser energy absorption and melting behavior during selective laser melting of titanium-matrix composite: role of ceramic addition. J Phys D Appl Phys 2021;54:115103. https://doi.org/10.1088/1361-6463.
[18] Wongchadakul P, Rattanadecho P, Wessapan T. Simulation of temperature distribution in different human skin types exposed to laser irradiation with different wavelengths and laser irradiation intensities. Songklanakarin J Sci Technol 2019;41:529–38. https://www.thaiscience.info/Journals/Article/SONG/10993161.pdf.
[19] Orimi HE, Jagadeesh S, Narayanswamy S. Experimental investigation of texturing complex geometry using high repetition nano laser and comparison with the simulated COMSOL model. Laser-Based Micro- and Nanoprocessing Xii 2018;10520:105201X. https://doi.org/10.1117/12.2298770.
[20] Ma JW, He GZ, Jia ZY, Wang XL, Wang JC. Solution of maximum laser ablation depth based on dynamic energy distribution model. Mater Manuf Process 2019;34:1719–25. https://doi.org/10.1080/10426914.2019.1666987.
[21] Moradi M, Moghadam MK, Shamsborhan M, Beiranvand ZM, Rasouli A, Vahdati M, et al. Simulation, statistical modeling, and optimization of CO2 laser cutting process of polycarbonate sheets. Optik 2021;225:164932. https://doi.org/10.1016/j.ijleo.2020.164932.
[22] Otto A, Schmidt M. Towards a universal numerical simulation model for laser material processing. Physics Procedia 2010;5:35–46. https://doi.org/10.1016/j.phpro.2010.08.120.
[23] Criales LE, Orozco PF, Medrano A, Rodriguez CA, Ozel T. Effect of fluence and pulse overlapping on fabrication of microchannels in PMMA/PDMS via UV laser micromachining: modeling and experimentation. Mater Manuf Process 2015;30:890–901. https://doi.org/10.1080/10426914.2015.1004690.
[24] Peligrad AA, Zhou E, Morton D, Li L. A melt depth prediction model for quality control of laser surface glazing of inhomogeneous materials. Optics & Laser Technology 2001;33:7–13. https://doi.org/10.1016/s0030-3992(00)00107-9.
[25] Salim MS, Ibrahim TK, Fouad S. Novel improvement glazing depth measurement model for concrete surface treated by CO2 laser. Optik 2017;142:412–20. https://doi.org/10.1016/j.ijleo.2017.06.019.
[26] Wu JZ, Wei HY, Yuan FB, Zhao PH, Zhang Y. Effect of beam profile on heat and mass transfer in filler powder laser welding. J Mater Process Technol 2018;258:47–57. https://doi.org/10.1016/j.jmatprotec.2018.03.011.
[27] Holman JP. Heat transfer. McGraw-Hill; 1986.
[28] Alimardani M, Toyserkani E, Huissoon JP. Three-dimensional numerical approach for geometrical prediction of multilayer laser solid freeform fabrication process. J Laser Appl 2007;19:14–25. https://doi.org/10.2351/1.2402518.
[29] Baird CS. Absorption of electromagnetic radiation. Access Sci 2019. https://doi.org/10.1036/1097-8542.001600.
[30] Ready JF, Farson DF, Feeley T. LIA handbook of laser materials processing. Springer Berlin, Heidelberg; 2001.
[31] Li JY, Li HN, Liao ZR, Axinte D. Analytical modelling of full single-track profile in wire-fed laser cladding. J Mater Process Technol 2021:290. https://doi.org/10.1016/j.jmatprotec.2020.116978.
[32] Malkin S. Grinding technology theory and applications of machining with abrasives. Dearborn: Society of Manufacturing Engineers; 2002.
[33] Advanced Diamond Technologies. D Materials, German. https://www.diamond-materials.com/en/products/; 2023.
[34] Han's laser. Shenzhen: HsLT Centre; 2023. https://www.hanslaser.com/pro-high cuting.html.